Supporting Information

Role of Oxygen Vacancy Ordering and Channel Formation in Tuning Intercalation Pseudocapacitance in Mo Single-Ion Implanted CeO_{2-x} Nanoflakes

Xiaoran Zheng,[a] Sajjad S. Mofarah,[a]* Alan Cen,[a] Claudio Cazorla,[a,c] Enamul Haque,[d] Ewing Y. Chen,[a] Armand J. Atanacio,[b] Madhura Manohar,[b] Corey Vutukuri,[a] Joel Luke Abraham,[a] Pramod Koshy,[a]* Charles C. Sorrell[a]*

[a] School of Materials Science and Engineering, UNSW Sydney, Sydney, NSW 2052, Australia
[b] Centre for Accelerator Science, Australian Nuclear Science and Technology Organisation, New Illawarra Road, Lucas Heights, NSW 2234, Australia
[c] Now at Departament de Física, Universitat Politècnica de Catalunya, Campus Nord B4-B5, 08034 Barcelona, Spain
[d] EH Solid State Physics Laboratory, Mymensingh, 2233 Gaffargaon, Bangladesh

[*] Corrseponding Authors:Xiaoran Zheng, Email: xiaoran.zheng@unsw.edu.au; Sajjad S. Mofarah: s.seifimofarah@unsw.edu.au; Pramod Koshy, Email: koshy@unsw.edu.au

EXPERIMENTAL SECTION

Sample Fabrication*:* Modified cathodic chronopotentiometric electrodeposition (MCCE) was done using a classical three-electrode configuration system. Ni foam with a true porosity of ~96% (Wuhan Geao Scientific Education Instrument, Wuhan, China), platinum (Basi Inc., Evansville, IN, USA, coil wire L = 23 cm, Ø = 0.5 mm), and Ag/AgCl (Basi Inc., Evansville, IN, USA) were used as the working, counter, and reference electrodes, respectively. All potentials were based on the Ag/AgCl reference electrode. The electrolyte was prepared by mixing $Ce(NO_3)_6 \cdot 6H_2O$ (0.1 M; 99.0%) and (NH_4NO_3) (0.1 M; ≥99.0%), which were purchased from Sigma Aldrich (City, Country), in 100 mL of deionised (DI) water . The pH was adjusted to 6 using 1 M NaOH, also obtained from the same supplier. Prior to electrodeposition, the Ni foam substrate was cleaned by ultrasonication in HCl (1 M) for 10 min, followed by rinsing with (DI) water and drying with compressed nitrogen. The nominal dimensions of the Ni foam were 10 mm × 5 mm × 2 mm. The potentiostat (EZstat Pro, Nuvant Systems, Crown Point, IN, USA) had a resolution of 300 μV and 3 nA in the ±100 μA range. The electrodeposited samples were stored in a desiccator with silica gel prior to analysis. The electrodeposition was done at –1 V *vs* Ag/AgCl for 20 min and the temperature of the electrolyte was held at 65°C using a water bath.

Mo Ion Implantation*:* Mo ion implantation under vacuum was done using the low-energy ion-implantation (LEII) beamline attached to the SIRIUS 6 MV accelerator at the Australian Nuclear Science and Technology Organization (ANSTO), as shown in **Figure S1**. The Dynamic-TRIM software code was used prior to experimentation in order to determine the implantation energy required for implantation depths of 20-40 nm. To this end, an accelerating energy of 10 keV and a dosage of 1×10^{15} atoms·cm^{-2} were used. The LEII implanter system operates using a Penning sputter source to

generate and extract the required ions from solid cathode targets. These ions are mass separated using a 90° electromagnet and subsequently focussed by electrostatic Einzel and quadrupole lenses onto the sample located in the end station experiment chamber. The beam then is electrostatically raster-scanned over the sample to perform implantation under a vacuum of 1×10^{-4} Pa. Since the amount of CeO_2 deposit was so small, quantitative analysis to determine the Mo dopant concentration was not possible. Consequently, it was calculated using the Mo dosage (1×10^{15} atoms·cm^{-2}), the weight gain from CeO_2 formation on all Ni surfaces (0.15 mg), image analysis (4 mm x 4 mm SEM image; *Image J* image analysis) to determine the 2D solid cross sectional area of the Ni foam (74 areal%), and halving this amount in order to account for ion implantation only on the top half of the foam struts. This calculation yields an Mo dopant concentration of ~1.7 mol%, which is similar that that used in other studies reported the effects of Mo doping by more conventional methods (1.0-2.0 mol%).[1-3]

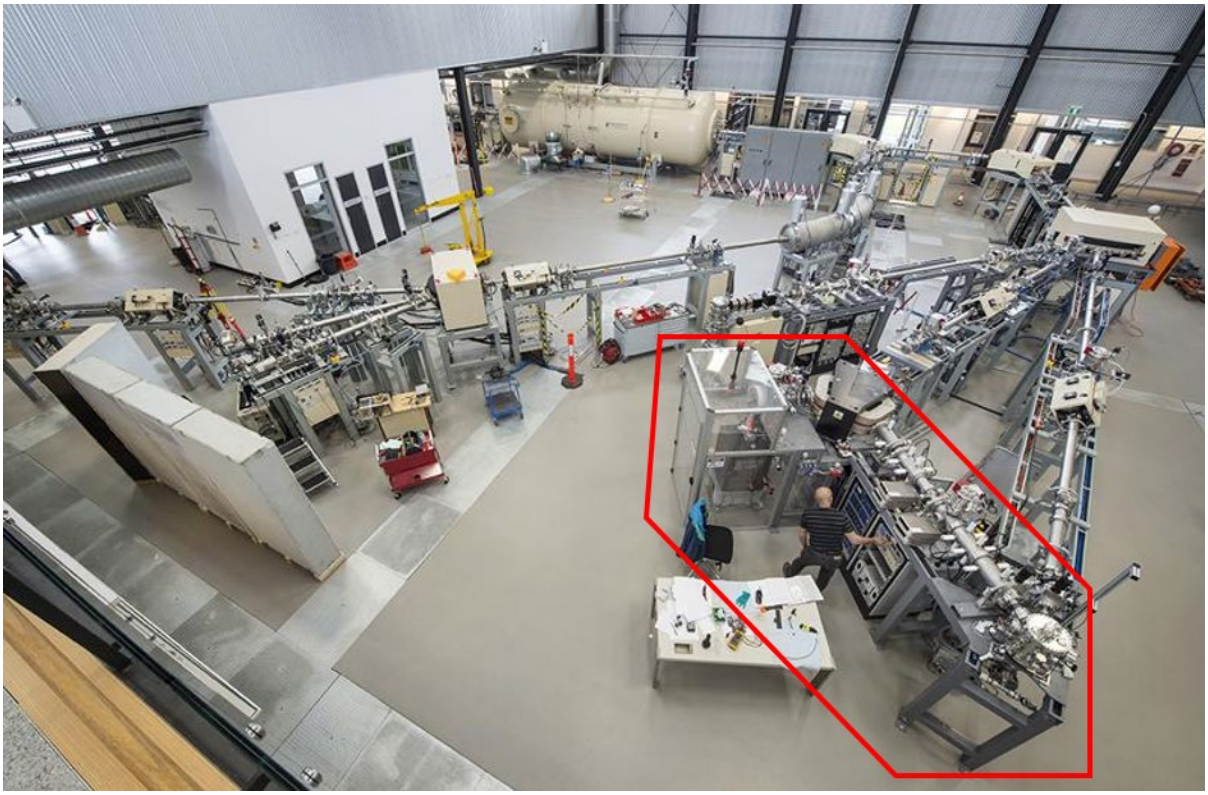

Figure S1 Photo of SIRIUS 6 MV accelerator at the Australian Nuclear Science and Technology Organization (ANSTO) with the Low Energy Ion Implanter system outlined in red.

Materials Characterisation*:* Mineralogical and defect data for the films were obtained by laser Raman microspectroscopy (Raman; Renishaw in Via Raman microscope, Wotton-under-Edge, Gloucestershire, UK, beam diameter 1.5 µm), which was equipped with a 35 mW helium-neon green laser (514 nm) in the range 200-800 cm^{-1}. The spectra were fitted and calibrated using Renishaw WiRE 4.3 software. The nanostructures of the samples were analysed using high-resolution transmission electron microscopy (HRTEM; Philips CM 200, Eindhoven, Netherlands, accelerating voltage 5 kV)

and selected area electron diffraction (SAED). Nanostructural images were obtained by scanning electron microscopy (SEM; FEI Nova NanoSEM, Hillsboro, OR, USA, secondary electron emission, accelerating voltage 5 kV). Local chemical analyses were done using energy dispersive spectroscopy (EDS; Hillsboro, OR, USA). Surface chemical analyses and defect data were obtained using X-ray photoelectron spectroscopy (XPS; ESCALAB 250Xi spectrometer, Thermo Fisher Scientific, Loughborough, Leicestershire, UK, 13 kV, 12 mA, spot size 500 μm). Defect data also were obtained using photoluminescence spectroscopy (PL; RF-5301PC spectrofluorophotometer, Shimadzu, Kyoto, Japan). The thickness was assessed by atomic force microscopy (AFM; Bruker Dimension Icon SPM, Bruker, Billerica, MA, USA, tapping mode, nominal tip radius 7 nm). A Bruker ScanAsyst-Air probe was installed with the AFM holder and used for all measurements. The scan size was set at 10 μm with an aspect ratio of 4. The pixel resolution was 512 samples/line for all scans. The scan rate was ~0.195 Hz since this slow scan rate ensured greater accuracy of the measurements. The chemical species present in the Ni foam were detected using Fourier transform infrared spectroscopy (FTIR; Spotlight 400 FTIR, PerkinElmer, Waltham, MA, USA) in the wavelength range 450-4000 cm^{-1}. The solubility of Mo was confirmed using proton-induced X-ray emission (PIXE; 2MV STAR tandem accelerator, High Voltage Engineering Europa, Amersfoort, Netherlands) with 2.6 MeV protons and ~10-15 nA current. The X-rays were detected using an Si(Li) detector fitted with a standard 25 μm thickness Be window and additional pinhole filter to decrease further the intensity of the X-rays excited by the low-Z elements with high cross sections; a 50 μC charge was acquired for each sample.

First Principles Calculations*:* Structural optimisations were performed using the full-potential, linearised, augmented, plane-wave method, as implemented in the WIEN2k code.[4,5] A non-shifted 10 × 10 × 10 k-point mesh, with RK_{max} = 7.0; muffin tin radii of 2.3 and 1.98 Bohr for Ce and O ions, respectively; and the semi-local Perdew-Burke-Ernzerhof (PBE) energy functional were used to determine the ground state structures of stoichiometric and nonstoichiometric CeO_{2-x}.[6,7] The calculations were performed on a supercell containing 24 atoms for the pristine (stoichiometric) system. Ground-state nonstoichiometric configurations were determined by exploring all possible oxygen vacancy arrangements in the pristine Ce_8O_{16} simulation cell.[8] Accurate densities of states and other electronic properties were obtained using spin-polarised single-point energy calculations on the geometries determined at the PBE functional level using a nonshifted 50 × 50 × 50 k-point mesh and modified Tran-Blaha Becke-Johnson energy functional (TB-mBJ).[9-11] These TB-mBJ results then were used with the modified-BoltzTraP code,[12] which solves the Boltzmann transport equation, in order to calculate electronic conductivities. Electron-phonon dynamical matrices were computed using the Quantum Espresso code in order to estimate charge carrier relaxation times.[13] For these types of calculations, ultrasoft pseudopotentials (from PP library v1.0), 888 k-points, an energy cut-off of 38 Ry, and a Methfessel-Paxton first-order smearing of 0.03 Ry were used.[14] The average electron-phonon dynamical matrices then were calculated using the EPA code.[15] Finally, the ionic diffusivities of oxygen

ions were estimated as a function of composition and temperature (300°-1200°C) using the classical molecular dynamics code LAMMPS and the CeO_2 force field reported in previous work.[16,17]

Spin-polarized First Principles calculations for Band Energy : Density functional theory (DFT) calculations were carried out to theoretically characterize the electronic properties of Mo dopants (substitutional and interstitial) and oxygen vacancies in CeO_2.[18] The PBEsol functional as it is implemented in the VASP software was used.[19,20] A "Hubbard-*U*" scheme with $U = 3$ eV was employed for a better treatment of the localized Ce 4*f* and Mo 4*d* electronic orbitals. The "projector augmented wave" method was used to represent the ionic cores by considering the following electrons as valence: Ce 4*f*, 5*d*, 6*s*, and 4*d*; Mo 4*d* and 5*s*; and O 2*s* and 2*p*.[21,22] Wave functions were represented in a plane-wave basis truncated at 650 eV. For integrations within the first Brillouin zone a Monkhorst-Pack k-point grid was used with a density equivalent to that of 16 × 16 × 16 for the fluorite CeO_2 unit cell. Periodic boundary conditions were applied along the three lattice vectors defining the simulation supercell; geometry relaxations were performed with a conjugate-gradient algorithm that optimized the ionic positions and the volume and shape of the simulation cell. The relaxations were halted when the forces in the atoms were all below 0.01 $eV \cdot Å^{-1}$. By using these technical parameters, the obtained energies were converged to within 0.5 meV per formula unit. The range-separated hybrid HSE06 exchange-correlation functional was employed to accurately estimate the electronic energy levels of the equilibrium geometries generated with the PBE sol+*U* functional.[23] The value of the theoretical valence and conduction energy band edges referred to the Fermi energy level were determined through analysis of the projected densities of electronic states obtained in the DFT calculations. A conventional CeO_2 fluorite unit cell containing 12 ions (with chemical formula Ce_4O_8) was used in all our DFT simulations. The Mo interstitial and substitutional concentrations were fixed to 20% and the position of the interstitial ions coincided with the high-symmetry octahedral fluorite sites (½,½,½) in pseudo-Cartesian notation. The reduced species Mo^{5+} and Mo^{4+} (charged oxygen vacancies) were generated by adding supplementary (removing) electrons to (from) the system.

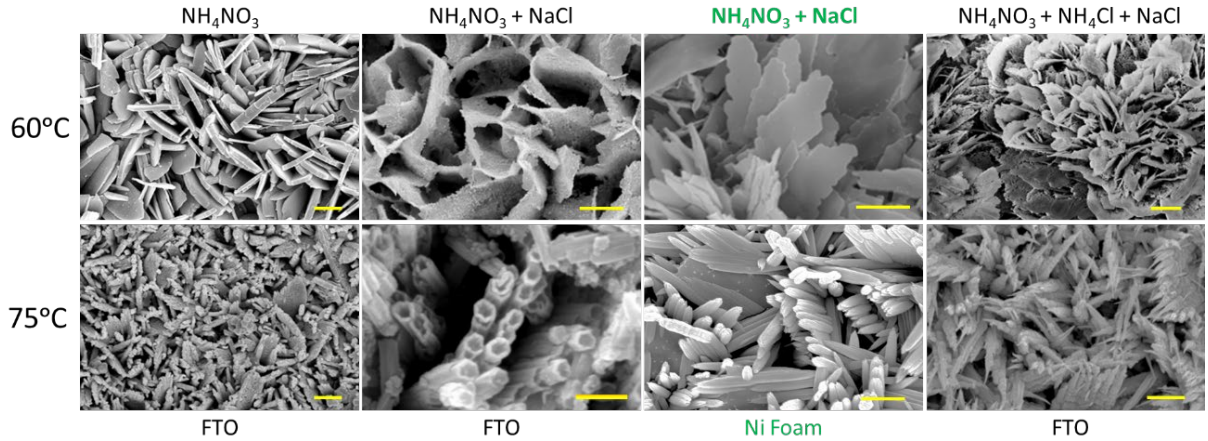

Figure S2 SEM images of different morphologies CeO_{2-x} as a function of experimental parameters (precursor type, temperature, substrate type) (scale bar = 300 nm)

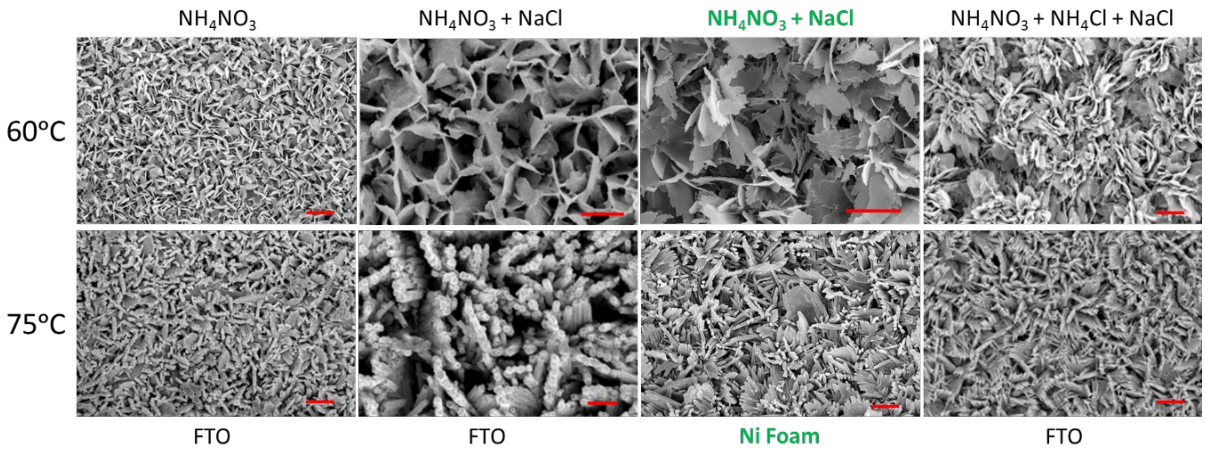

Figure S3 Enlarged SEM images of **Figure S2** (scale bar = 3 μm)

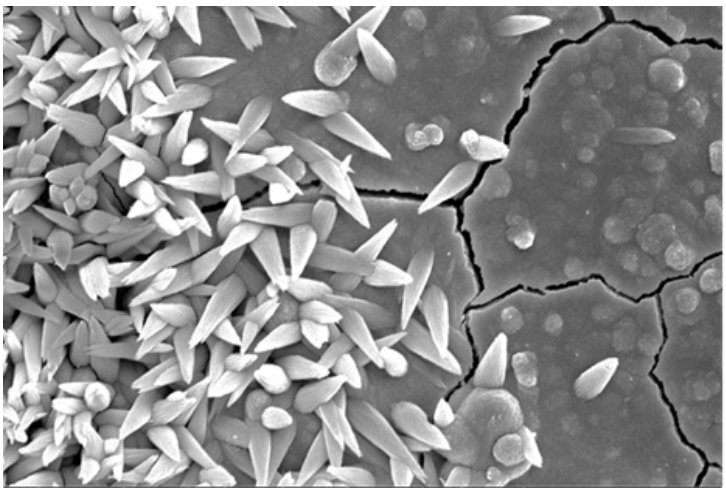

Figure S4 Ni foam with as-electrodeposited CeO_{2-x} after 5 min (left) and cracked surface layer (right)

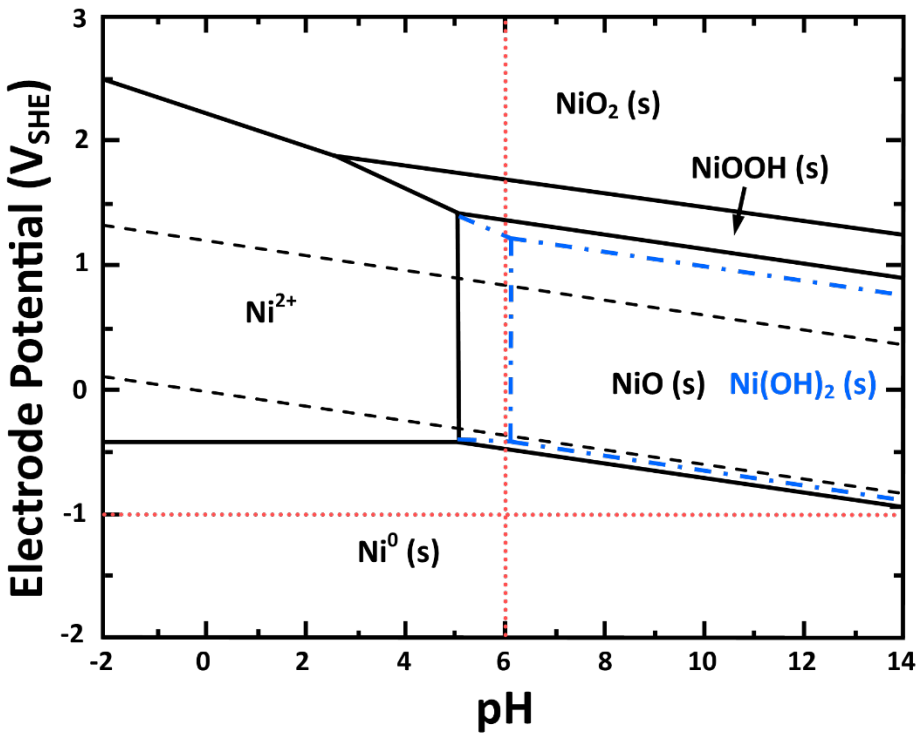

Figure S5 Ni – H_2O Pourbaix diagram ($Ni(OH)_2$ predominance region overlaps (blue dash-dot lines) because both NiO (s) and $Ni(OH)_2$ occur simultaneously), adapted from [24] (NiO red dotted line = experimental conditions)

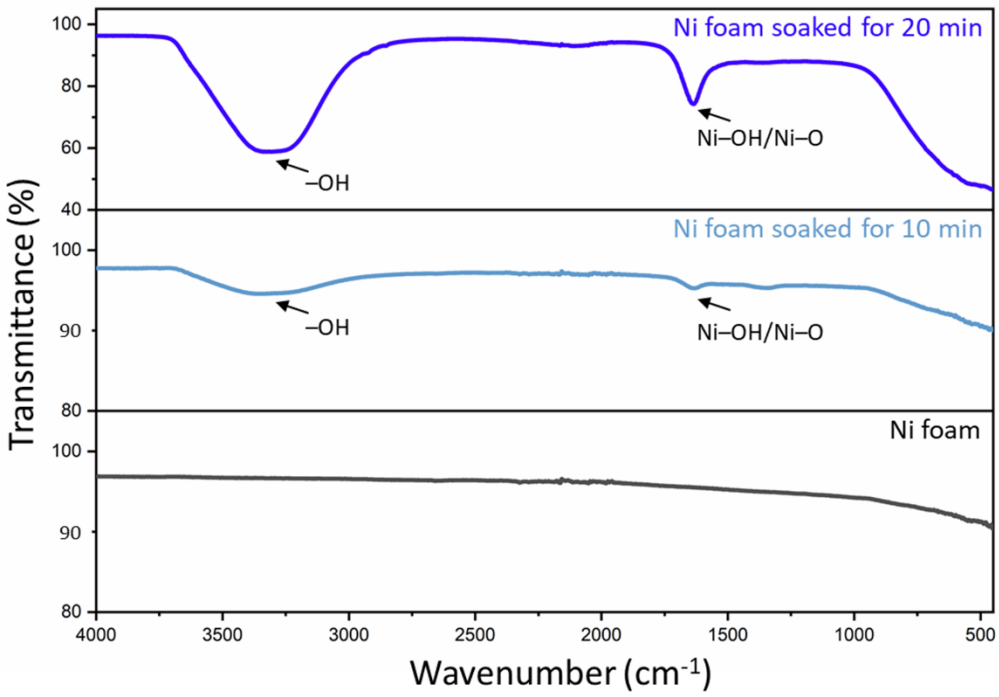

Figure S6 FTIR data of Ni foam soaked for 0, 10 and 20 min.

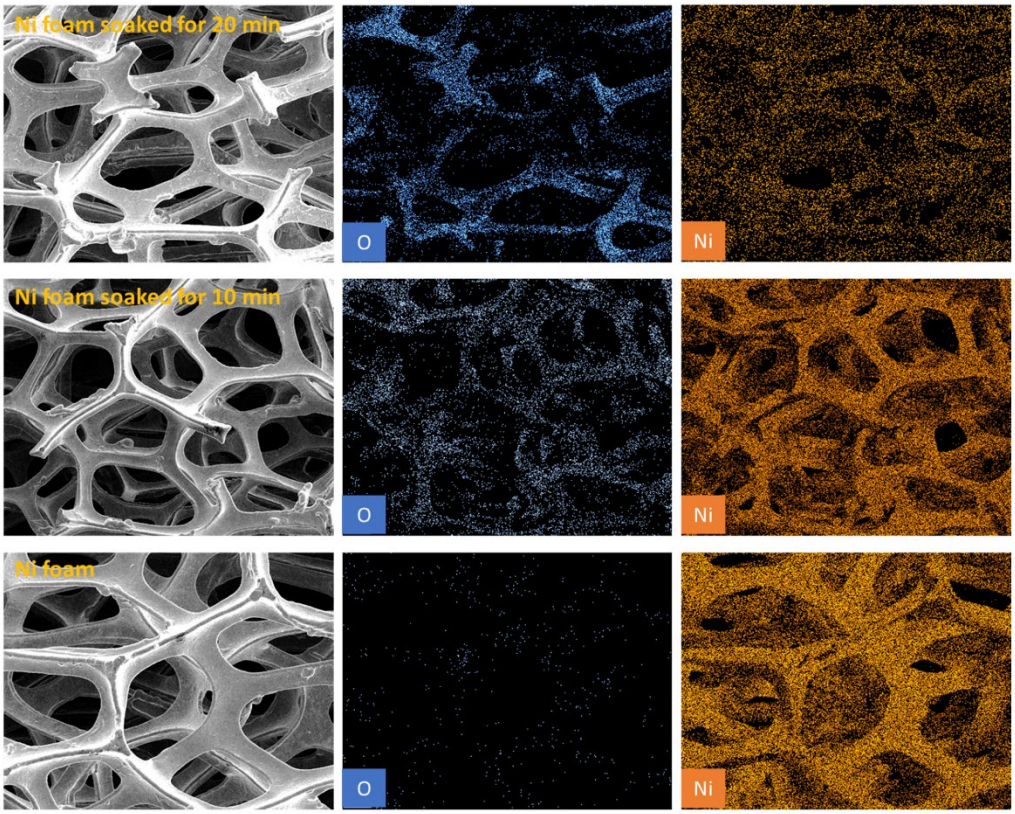

Figure S7 EDS mapping of Ni foam soaked for 0, 10, and 20 min

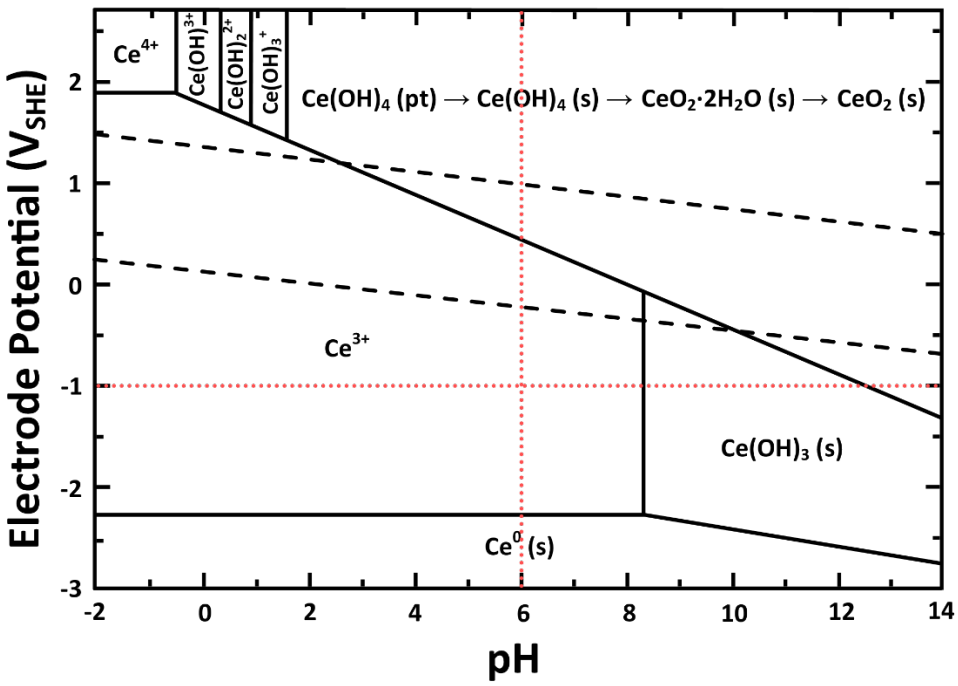

Figure S8 Ce – H_2O Pourbaix diagram, adapted from [25]

Table S1. Potential extrinsic defect equilibria for Mo- or Ni-doped of CeO_{2-x}.[26]

Dopant	Solid Solubility	Process	Extrinsic Defect Equilibria
Mo	Substitutional	Ionic Charge Compensation	$4Mo_{Mo}^{x} + 10O_{O}^{x} \xrightarrow{CeO_2} 4Mo_{Ce}^{\bullet} + V_{Ce}^{''''} + 5Ce_{S}^{x} + 10O_{O}^{x}$
		Electronic Charge Compensation	$2Mo_{Mo}^{x} + 5O_{O}^{x} \xrightarrow{CeO_2} 2Mo_{Ce}^{\bullet} + 2Ce_{S}^{x} + 4O_{O}^{x} + ½O_2\ (g) + 2e'$
		Redox Charge Compensation	$2Mo_{Mo}^{x} + 5O_{O}^{x} \xrightarrow{CeO_2} 2Mo_{Ce}^{\bullet} + 2Ce_{S}^{x} + 4O_{O}^{x} + ½O_2\ (g) + 2Ce_{Ce}'$
	Interstitial	Ionic Charge Compensation	$4Mo_{Mo}^{x} + 10O_{O}^{x} \xrightarrow{CeO_2} 4Mo_{i}^{\bullet\bullet\bullet\bullet} + 5V_{Ce}^{''''} + 5Ce_{S}^{x} + 10O_{O}^{x}$
		Electronic Charge Compensation	$2Mo_{Mo}^{x} + 5O_{O}^{x} \xrightarrow{CeO_2} 2Mo_{i}^{\bullet\bullet\bullet\bullet\bullet} + 4O_{O}^{x} + ½O_2\ (g) + 10e'$
		Redox Charge Compensation	$2Mo_{Mo}^{x} + 5O_{O}^{x} \xrightarrow{CeO_2} 2Mo_{i}^{\bullet\bullet\bullet\bullet\bullet} + 4O_{O}^{x} + ½O_2\ (g) + 10Ce_{Ce}'$
Ni	Substitutional	Ionic Charge Compensation	$Ni_{Ni}^{x} + O_{O}^{x} \xrightarrow{CeO_2} Ni_{Ce}^{''} + V_{O}^{\bullet\bullet} + Ce_{S}^{x} + ½O_2\ (g)$
		Electronic Charge Compensation	$Ni_{Ni}^{x} + O_{O}^{x} + ½O_2\ (g) \xrightarrow{CeO_2} Ni_{Ce}^{''} + 2O_{O}^{x} + Ce_{S}^{x} + 2h^{\bullet}$
		Redox Charge Compensation	$Ni_{Ni}^{x} + O_{O}^{x} \xrightarrow{CeO_2} Ni_{Ce}^{''} + Ce_{S}^{x} + O_{O}^{x} + 2Ce_{Ce}^{\bullet}$
	Interstitial	Ionic Charge Compensation	$2Ni_{Ni}^{x} + 2O_{O}^{x} \xrightarrow{CeO_2} 2Ni_{i}^{\bullet\bullet} + V_{Ce}^{''''} + Ce_{S}^{x} + 2O_{O}^{x}$
		Electronic Charge Compensation	$Ni_{Ni}^{x} + O_{O}^{x} + ½O_2\ (g) \xrightarrow{CeO_2} Ni_{i}^{\bullet\bullet} + 2O_{O}^{x} + 2e'$
		Redox Charge Compensation	$Ni_{Ni}^{x} + O_{O}^{x} + ½O_2 \xrightarrow{CeO_2} Ni_{i}^{\bullet\bullet} + 2O_{O}^{x} + 2Ce_{Ce}'$

M_{M}^{x}	=	Metal on metal lattice site	(0 charge)
O_{O}^{x}	=	Oxygen ion on oxygen lattice site	(0 charge)
$M_{M\dagger}^{\bullet}$	=	Donor dopant (M) metal substitution on metal lattice site (M†)	(+ charge)
$M_{M\dagger}'$	=	Acceptor dopant (M) metal substitution on metal lattice site (M†)	(– charge)
$M_{i}^{\bullet}$	=	Metal in interstitial site	(+ charge)
M_{S}^{x}	=	Metal removed from lattice by charge compensation and neutralisation at surface	(0 charge)
V_{M}'	=	Metal vacancy	(– charge)
$V_{O}^{\bullet\bullet}$	=	Oxygen vacancy	(+ charge)
Ce_{Ce}'	=	$Ce^{4+} \rightarrow Ce^{3+}$ reduction	(– charge)
$Ce_{Ce}^{\bullet}$	=	$Ce^{3+} \rightarrow Ce^{4+}$ oxidation	(+ charge)
e'	=	Electron	(– charge)
$h^{\bullet}$	=	Hole	(+ charge)
$½O_2$	=	Oxygen gas filling or removed from $V_{O}^{\bullet\bullet}$	(0 charge)

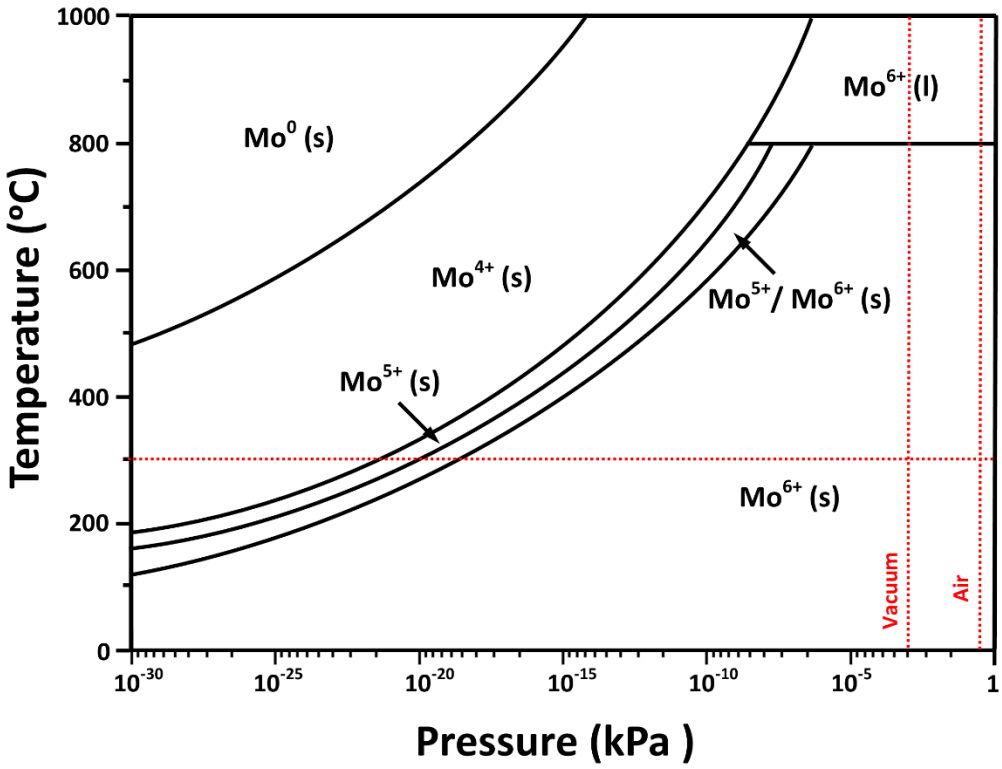

Figure S9 Mo thermodynamic stability diagram (calculated using FactSage)

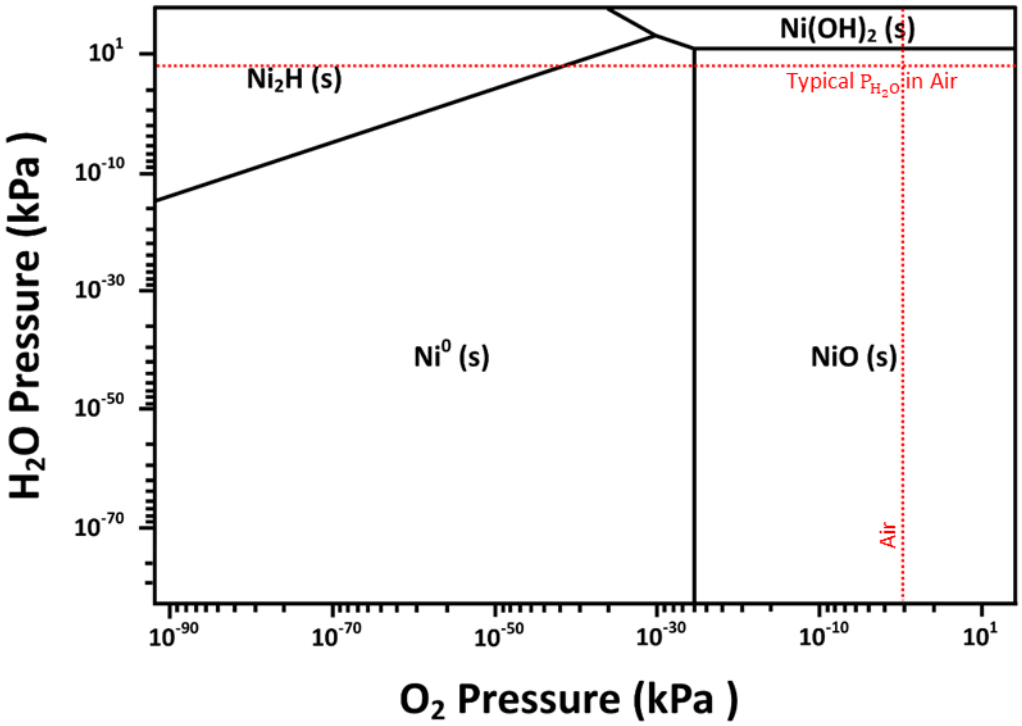

Figure S10 Ni $P_{H_2O} - P_{O_2}$ thermodynamic stability diagram at 300°C (calculated using FactSage)

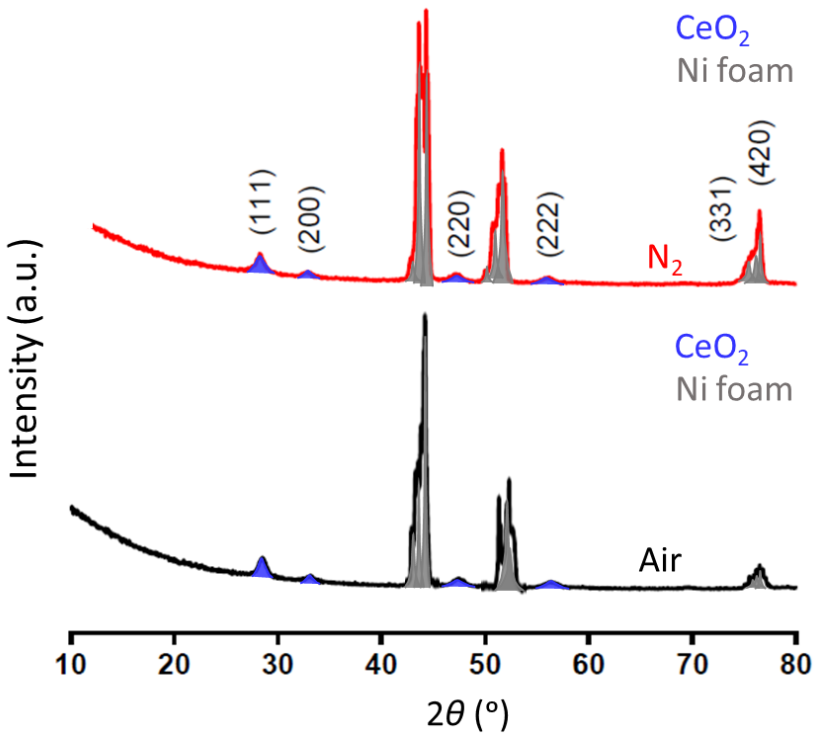

Figure S11 XRD patterns of Air and N_2 on Ni foam (identical intensity scales)

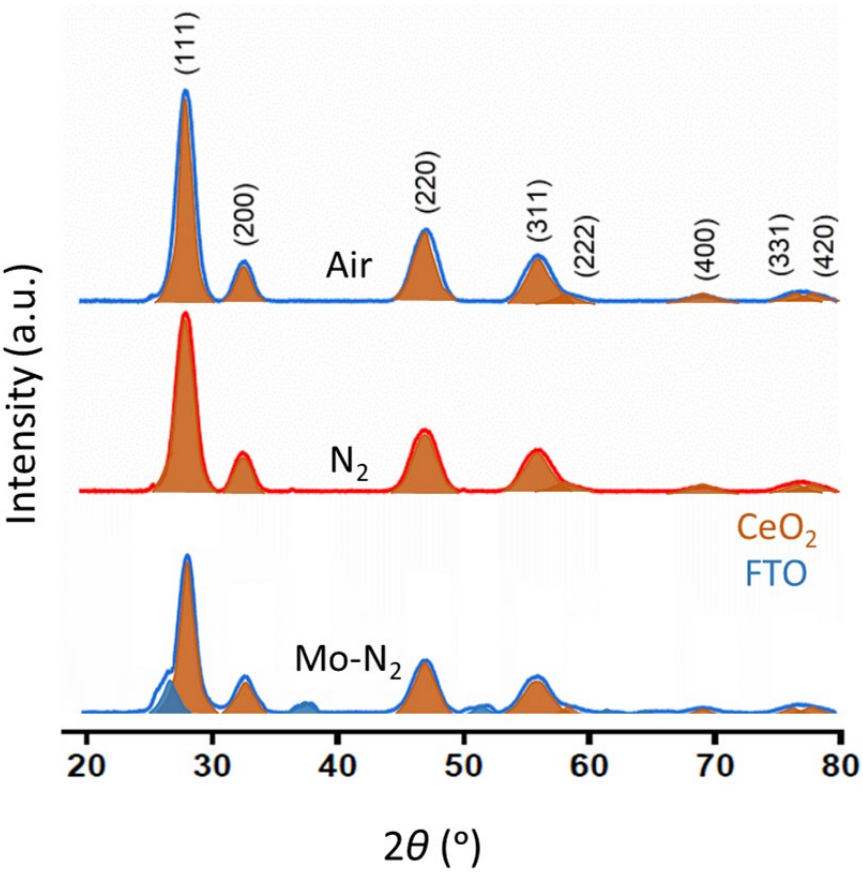

Figure S12 XRD patterns of Air, N_2, and Mo-N_2 on FTO (identical intensity scales)

Table S2 Lattice parameters calculated by Rietveld refinement from XRD data and F_{2g} peak positions from Raman data for Air, N_2 and Mo-N_2 (goodness of fit ≈ 5)

Sample	Lattice Parameter (nm)	F_{2g} Peak Position (cm^{-1})	Relative Shift (cm^{-1})	Surface Stress State
Air	0.5445	461.71	--	--
N_2	0.5421	459.91	–1.18	Tension
Mo-N_2	0.5201	458.71	–3.00	Tension

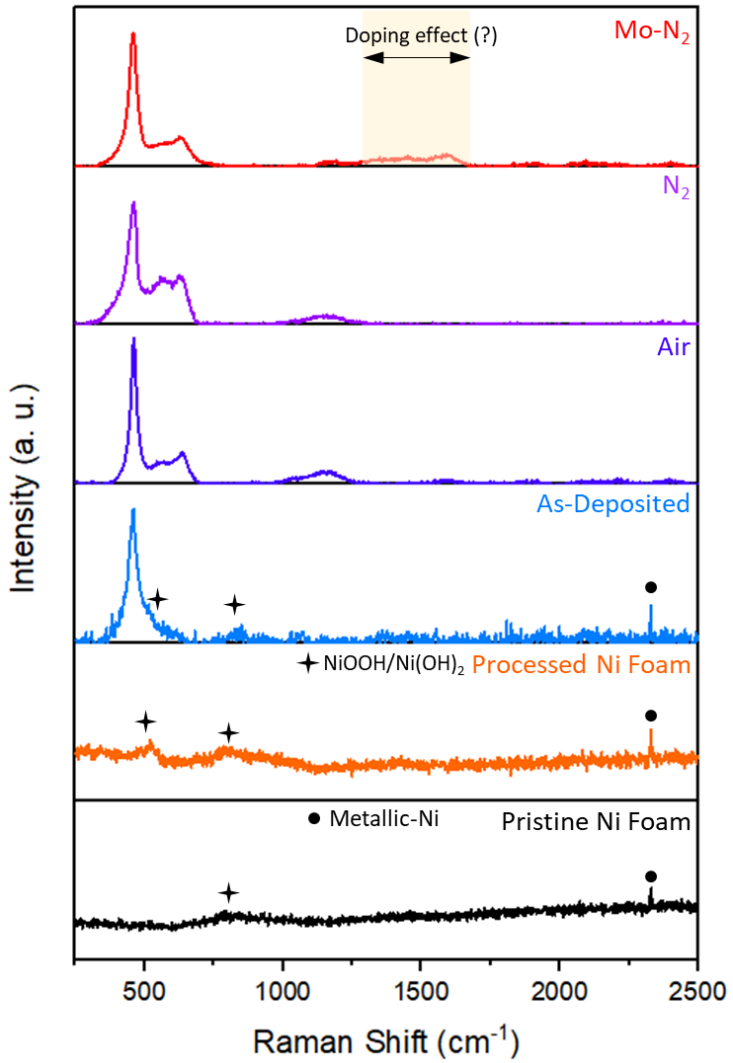

Figure S13 Laser Raman microspectra (the patterns for NiOOH and $Ni(OH)_2$ cannot be differentiated)

Comparison of the microspectra for Mo-N_2 with those for Air and N_2 reveals shifts in the major F_{2g} peak and the appearance of new peaks in the range 1300-1650 cm^{-1}. The peak at 1360 cm^{-1} is assigned as the 3LO mode (third overtone band of longitudinal optic mode).[27] These peaks have been observed previously for doped CeO_{2-x}, albeit for other dopant ions.[27-30]

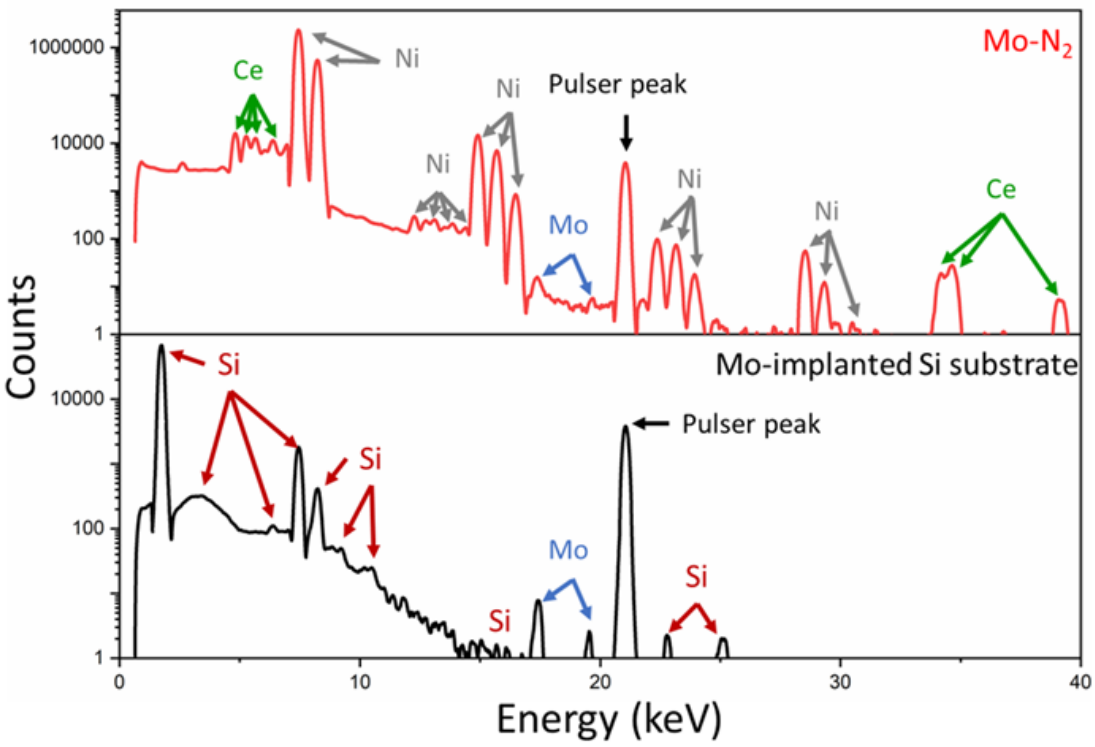

Figure S14 Proton Induced X-ray Emission Spectroscopy (PIXE)

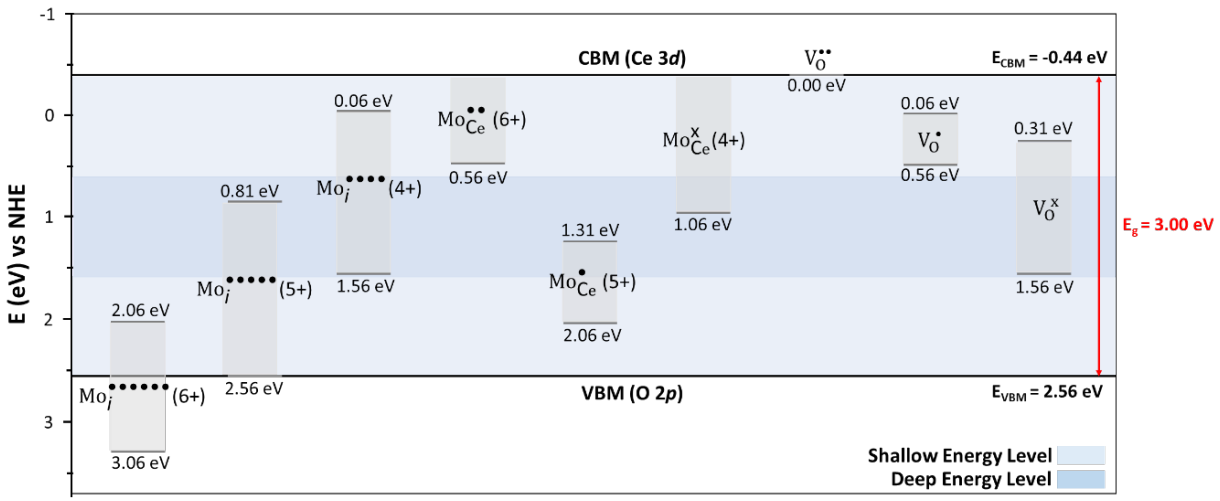

Figure S15 Comprehensive defect energy level diagram for intrinsic and extrinsic defects of different valence states for Mo-doped CeO_2 based on spin-polarized DFT calculations

Table S3 Summary of work on pure and doped of CeO_2 for supercapacitors

Row	Sample	Specific Capacitance	Capacitance after Cycling	Ref.
1	CeO_2-Ni foam	582 $F \cdot g^{-1}$ at 1mV$\cdot s^{-1}$	92.0% after 2000 cycles	Present work
2	Undoped CeO_2	135 $F \cdot g^{-1}$ at 1 $A \cdot g^{-1}$	92.5% after 1000 cycles	31
3	CeO_2-Ni foam	225 $F \cdot g^{-1}$ at 5 mV$\cdot s^{-1}$	--	32
4	CeO_2 nanoparticles/graphene	208 $F \cdot g^{-1}$ at 1 $A \cdot g^{-1}$	97.6% after 1000 cycles	33
5	CeO_2-5% graphene	110 $F \cdot g^{-1}$ at 10 mV$\cdot s^{-1}$	--	34
6	CeO_2 nanoparticles/graphene	208 $F \cdot g^{-1}$ at 1 $A \cdot g^{-1}$	97.0% after 2000 cycles	27
7	Reduced graphene oxide (rGO) /CeO_2	265 $F \cdot g^{-1}$ at 5 mV$\cdot s^{-1}$	96.0% after 1000 cycles	35
8	CeO_2 mesoporous microspheres	142.5 $F \cdot g^{-1}$ at 0.25 $A \cdot g^{-1}$	75.0% after 1000 cycles	36
9	Hollow CeO_2 nanospheres on graphitic carbon	501 $F \cdot g^{-1}$ at 1 $A \cdot g^{-1}$	93.0% after 5000 cycles	37
10	Mo (0.01 mol%)-CeO_2-Ni foam	746 $F \cdot g^{-1}$ at 1 mV$\cdot s^{-1}$	95.0% after 2000 cycles	Present Work
11	Ni-doped CeO_2	446 $F \cdot g^{-1}$ at 1 $A \cdot g^{-1}$	97.5% after 2000 cycles	38
12	Mg-doped CeO_2	432 $F \cdot g^{-1}$ at 1 $A \cdot g^{-1}$	89.0% after 10,000 cycles	39
13	Ni-doped CeO_2	577 $F \cdot g^{-1}$ at 2 $A \cdot g^{-1}$	94.0% after 1000 cycles	40
14	carbon/Ni-doped CeO_2	253 $F \cdot g^{-1}$ at 0.25 $A \cdot g^{-1}$	94.0% after 1000 cycles	41
15	CeO_2–SnO_2/rGO-Ni foam	156 $F \cdot g^{-1}$ at 0.5 $A \cdot g^{-1}$	92.0% after 1000 cycles	42
16	Zn-doped CeO_2 quantum dots	358 $F \cdot g^{-1}$ at 10 $A \cdot g^{-1}$	96.0% after 1000 cycles	43
17	CeO_2-α-MnO_2-rGO	466 $F \cdot g^{-1}$ at 1 $A \cdot g^{-1}$	100.0% after 10000 cycles	44
18	Co (5 mol%)-doped CeO_2	573 $F \cdot g^{-1}$ at 2 $A \cdot g^{-1}$	96.0% after 1000 cycles	45

REFERENCES

(1) Zhang, N.; Jalil, A.; Wu, D.; Chen, S.; Liu, Y.; Gao, C.; Ye, W.; Qi, Z.; Ju, H.; Wang, C.; Wu, X.; Song, L.; Zhu, J.; Xiong, Y.; Refining Defect States in $W_{18}O_{49}$ by Mo Doping: A Strategy for Tuning N_2 Activation Towards Solar-Driven Nitrogen Fixation. *JACS* **2018**, *140*, 9434-9443.

(2) Mai, L.Q; Chen, W.; Xu, Q.; Peng, J.F.; Zhu, Q.Y.; Mo Doped Vanadium Oxide Nanotubes: Microstructure and Electrochemistry. *Chem. Phys. Lett.* **2003**, *382*, 307-312.

(3) Büyükburç, A.; Aydinol, M.K. Effect of Cr and Mo Doping on the Electrochemical Properties of Freeze-Dried $LiCoO_2$. *Int. J. Mater. Res.* **2014**, *105*, 983-991.

(4) Blaha, P.; Schwarz, K.; Tran, F.; Laskowski, R.; Madsen, G.K.H.; Marks, L.D. WIEN2k: An APW+lo Program for Calculating the Properties of Solids. *J. Chem. Phys*. **2020**, *152*, No. 074101.

(5) Blaha, P.; Schwarz, K.; Madsen, G.K.H.; Kvasnicka, D.; Luitz, J.; Laskowski, R.; Tran, F.; Marks, L.D. (Karlheinz Schwarz, Techn. Universität Wien, Austria). WIEN2k: An Augmented Plane Wave Plus Local Orbitals Program for Calculating Crystal Properties. *ISBN 3-9501031-1-2*, **2018**.

(6) Perdew, J.P.; Burke, K.; Ernzerhof, M. Generalized Gradient Approximation Made Simple. *Phys. Rev. Lett.* **1996**, *77*, No. 3865.

(7) Perdew, J.P.; Ruzsinszky, A.; Csonka, G.I.; Vydrov, O.A.; Scuseria, G.E.; Constantin, L.A.; Zhou, X.; Burke, K. Restoring the Density-Gradient Expansion for Exchange in Solids and Surfaces. *Phys. Rev. Lett.* **2008**, *100*, No. 136406.

(8) Duclos, S.J.; Vohra, Y.K.; Ruoff, A.L.; Jayaraman, A.; Espinosa, G.P. High-Pressure X-Ray Diffraction Study of CeO_2 to 70 GPa and Pressure-Induced Phase Transformation from the Fluorite Structure. *Phys. Rev. B* **1988**, *38*, No. 7755.

(9) Koller, D.; Tran, F.; Blaha, P. Improving the Modified Becke-Johnson Exchange Potential. *Phys. Rev. B-Condens. Matter Mater. Phys.* **2012**, *85*, No. 155109.

(10) Koller, D.; Tran, F.; Blaha, P. Merits and Limits of the Modified Becke-Johnson Exchange Potential, *Phys. Rev. B* **2011**, *83*, No. 195134.

(11) Tran, F.; Blaha, P. Accurate Band Gaps of Semiconductors and Insulators with a Semilocal Exchange-Correlation Potential. *Phys. Rev. Lett.* **2009**, *102*, No. 226401.

(12) Madsen, G.K.H.; Singh, D.J. BoltzTraP. A Code for Calculating Band-Structure Dependent Quantities. *Comput. Phys. Commun.* **2006**, *175*, 67-71.

(13) Giannozzi, P.; Baroni, S.; Bonini, N.; Calandra, M.; Car, R.; Cavazzoni, C.; Ceresoli, D.; Chiarotti, G.L.; Cococcioni, M.; Dabo, I. QUANTUM ESPRESSO: A Modular and Open-Source Software Project for Quantum Simulations of Materials. *J. Phys. Condens. Matter.* **2009**, *21*, No. 395502.

(14) Methfessel, M.; Paxton, A.T. High-Precision Sampling for Brillouin-Zone Integration in Metals. *Phys. Rev. B* **1989**, *40*, No. 3616.

(15) Samsonidze, G.; Kozinsky, B. Accelerated Screening of Thermoelectric Materials by First-Principles Computations of Electron–Phonon Scattering. *Adv. Energy Mater.* **2018**, *8*, No. 1800246.

(16) Plimpton, S. Fast Parallel Algorithms for Short-Range Molecular Dynamics. *J Comp Phys*. **1995**, *117*, 1-19.

(17) Harrington, G.F.; Sun, L.; Yildiz, B.; Sasaki, K.; Perry, N.H.; Tuller, H.L. The Interplay and Impact of Strain and Defect Association on the Conductivity of Rare-Earth Substituted Ceria. *Acta Mater.* **2019**, *166*, 447-458.

(18) Cazorla, C.; Boronat, B. Simulation and Understanding of Atomic and Molecular Quantum Crystals. *Rev. Mod. Phys.* **2017**, *89*, No. 035003.

(19) Perdew, J.P.; Ruzsinszky, A.; Csonka, G.I.; Vydrov, O.A.; Scuseria, G.E.; Constantin, L.A.; Zhou, X.; Burke, K. Restoring the Density-Gradient Expansion for Exchange in Solids and Surfaces. *Phys. Rev. Lett.* **2008**, *100*, No. 136406.

(20) Kresse, G.; Furthmuller, J. Efficient Iterative Schemes for Ab Initio Total-Energy Calculations Using a Plane-Wave Basis Set. *Phys. Rev. B* **1996**, *54*, No. 11169.

(21) Dudarev,S.L.; Botton, G.A.; Savrasov, S.Y.; Humphreys, C.L.; Sutton, A.P. Electron-Energy-Loss Spectra and the Structural Stability of Nickel Oxide: An LSDA+U study. *Phys. Rev. B* **1998**, *57*, No. 1505.

(22) Blochl, P.E. Projector Augmented-Wave Method. *Phys. Rev. B* **1994**, *50*, No. 17953.

(23) Brothers, E.N.; Izmaylov, A.F.; Normand, J.O.; Barone, V.; Scuseria, G.E. Accurate Solid-State Band Gaps via Screened Hybrid Electronic Structure Calculations. *J. Chem. Phys.* **2008**, *129*, No. 011102.

(24) Huang, L.F.; Hutchison, M.; Santucci Jr, R.; Scully, J.R.; Rondinelli, J.M. Improved Electrochemical Phase Diagrams from Theory and Experiment: The Ni–Water System and Its Complex Compounds. *J. Phys. Chem. C* **2017**, *121*, 9782-9789.

(25) Xu, Y.; Mofarah, S.S.; Mehmood, R.; Cazorla, C.; Koshy, P.; Sorrell, C.C. Design Strategies for Ceria Nanomaterials: Untangling Key Mechanistic Concepts. *Mater. Horiz.* **2021**, *8*, 102-123.

(26) Zheng, X.; Mofarah, S.S.; Cazorla, C.; Daiyan, R.; Esmailpour, A.A.; Scott, J.; Yao, Y.; Lim, S.; Wong, V.; Chen, E.Y.; Arandiyan H.; Koshy, P.; Sorrell, C.C. Decoupling the Impacts of Engineering Defects and Band Gap Alignment Mechanism on the Catalytic Performance of Holey 2D CeO_{2-x}-Based Heterojunctions. *Adv. Funct. Mater.* **2021**, No. 2103171.

(27) Hao, Q.;Morton, S.M.; Wang, B.; Zhao, Y.; Jensen, L.; Huang, T.L. Tuning Surface-Enhanced Raman Scattering from Graphene Substrates Using the Electric Field Effect and Chemical Doping. *Appl. Phys. Lett.* **2013**, *102*, No. 011102.

(28) Wang, Y.; Guo, C.X.; Liu, J.; Chen, T.; Yang, H.; Li, C.M. CeO_2 Nanoparticles/Graphene Nanocomposite-Based High Performance Supercapacitor, *Dal. Trans.* **2011**, *40*, 6388-6391.

(29) Saravanan, T.; Shanmugam, M.; Anandan, P.; Azhagurajan, M.; Pazhanivel, K.; Arivanandhan, M.; Hayakawa, Y.; Jayavel, R. Facile Synthesis of Graphene-CeO_2 Nanocomposites with Enhanced Electrochemical Properties for Supercapacitors. *Dal. Trans.* **2015**, *44*, 9901-9908.

(30) Radović, M.B.; Dohcevic-Mitrovic, Z.; Paunović, N.M.; Scepanovic, M.; Matović, B.; Popović, Z.V. Effect of Fe^{2+} (Fe^{3+}) Doping on Structural Properties of CeO_2 Nanocrystals. *Adv. At. Mol. Opt. Phys.* **2009**, *116*, 84-87.

(31) Prasanna, K.; Santhoshkumar, P.; Jo, Y.N.; Sivagami, I.N.; Kang, S.H.; Joe, Y.C.; Lee, C.W. Highly Porous CeO_2 Nanostructures Prepared via Combustion Synthesis for Supercapacitor Applications. *Appl. Surf. Sci.* **2018**, *449*, 454-460.

(32) Hu, Y.M.; Shi, T.T.; Ni, J.S.; Jin, H.M.; Zhu, M.Y.; Li, Y.; Bai, Q. Super-Capacitive Performances of Nickel Foam Supported CeO_2 Nanoparticles. *J. Shanghai Jiaotong Uni. (Sci.)* **2012**, *17*, 513-516.

(33) Chakrabarty, N.; Dey, A.; Krishnamurthy, S.; Chakraborty, A.K. CeO_2/Ce_2O_3 Quantum Dot Decorated Reduced Graphene Oxide Nanohybrid as Electrode for Supercapacitor. *Appl. Surf. Sci.* **2021**, *536*, No. 147960.

(34) Padmanathan, N.; Selladurai, S. Shape Controlled Synthesis of CeO_2 Nanostructures for High Performance Supercapacitor Electrodes. *RSC Adv.* **2014**, *4*, 6527.

(35) Ji, Z.; Shen, X.; Zhou, H.; Chen, K. Facile Synthesis of Reduced Graphene Oxide/CeO_2 Nanocomposites and Their Application in Supercapacitors. *Ceram. Int.* **2015**, *41*, 8710-8716.

(36) Kumar, M.; Yun, J.H.; Bhatt, V.; Singh, B.; Kim, J.; Kim, J.S.; Kim, B.S.; Lee, C.Y. Role of Ce^{3+} Valence State and Surface Oxygen Vacancies on Enhanced Electrochemical Performance of Single Step Solvothermally Synthesized CeO_2 Nanoparticles. *Electrochimica Acta* **2018**, *284*, 709-720.

(37) Phokha, S.; Hunpratub, S.; Chanlek, N.; Sonsupap, S.; Maensiri, S. Synthesis, Characterization and Electrochemical Performance of Carbon/Ni-doped CeO_2 composites. *J. Alloys Compd.* **2018**, *750*, 788-797.

(38) Alex, J.; Rajkumar, S.; PrincyMerlin, J.; Aravind, A.; Sajan, D.; Praveen, C.S. Single Step Auto-Igniting Combustion Technique Grown CeO_2 and Ni-Doped CeO_2 Nanostructures for Multifunctional Applications. *J. Alloys Compd.* **2021**, *882*, No. 160409.

(39) Hussain, K.; Ali, I.; Hasnain, S.; Hussain, S.S.; Hussain, B.; Khan, M.S.; Ammar, S.M.; Hussain, B.; Hussain, A.; Javed, M.A.; Ullah, A. Reagents Assisted Mg-Doped CeO_2 for High-Performance Energy-Storage Applications. *J. Electroanal. Chem.* **2020**, *873*, No. 114401.

(40) Murugan, R.; Ravi, G.; Vijayaprasath, G.; Rajendran, S.; Thaiyan, M.; Nallappan, M.; Gopalan, M.; Hayakawa, Y. Ni–CeO_2 Spherical Nanostructures for Magnetic and Electrochemical Supercapacitor Applications. *Phys. Chem. Chem.* **2017**, *19*, 4396-4404.

(41) Sun, M.; Li, Z.; Li, H.; Wu, Z.; Shen, W.; Fu, Y.Q. *Electrochim. Acta*, **2020**, *331*, No. 135366.

(42) Kumar, G.S.; Reddy, S.A.; Maseed, H.; Reddy, N.R. Facile Hydrothermal Synthesis of Ternary CeO_2–SnO_2/rGO Nanocomposite for Supercapacitor Application. *Funct. Mater. Lett.* **2020**, *15*, No. 2051005.

(43) Ponnar, M.; Sathya, M.; Pushpanathan, K. Enhanced UV Emission and Supercapacitor Behavior of Zn Doped CeO_2 Quantum Dots. *Chem. Phys. Lett.* **2020**, 761, No. 138087.

(44) Xie, A.; Wang, H.; Zhu, Z.; Zhang, W.; Li, X.; Wang, Q.; Luo, S. Mesoporous CeO_2-α-MnO_2- Reduced Graphene Oxide Composite with Ultra-High Stability as A Novel Electrode Material for Supercapacitor. *Surf. Interfaces* **2021**, *25*, No. 101177.

(45) Murugan, R.; Ravi, G.; Yuvakkumar, R.; Rajendran, S.; Maheswari, N.; Muralidharan, G.; Hayakawa, Y. Pure and Co Doped CeO_2 Nanostructure Electrodes with Enhanced Electrochemical Performance for Energy Storage Applications. *Ceram. Int.* **2017**, *43*, 10494-10501.